



Methodology for Establishing Comprehensive Stress Paths in Rocks During Hollow Cylinder Testing

Zhen Li¹ · Hui Zhou² · Yue Jiang² · Dawei Hu² · Chuanqing Zhang²

Received: 23 June 2017 / Accepted: 13 October 2018 / Published online: 29 October 2018
© Springer-Verlag GmbH Austria, part of Springer Nature 2018

Abstract

We here systematically investigated the methodology for establishing comprehensive stress paths with the aim of developing hollow cylinder apparatuses for rock mechanics. The research was based on the stress combination in element of hollow cylinder sample with varied loading analysis treatment. For this purpose, we discussed the mechanism underlying the variations in principal stress magnitude and principal stress rotation. The orientation angle of the major principal stress was defined in an alternative prospect. Then a series of stress paths was introduced, including the hydrostatic pressure stress path, principal stress magnitude variation stress path on the deviatoric plane, pure principal stress rotation stress path, and the complex stress path coupling the variation in the magnitude of principal stress and principal stress rotation effect. The comprehensive stress paths were analyzed with rock mechanical theory and a mathematical approach. The suggested loading methods were examined using simulation loading tests, laboratory case tests and special case verification. The results showed successful completion of different stress paths. The proposed methodology was first investigated systematically in rock mechanics, contributing to development of the new hollow cylinder apparatus and complex rock engineering simulation.

Keywords Principal stress magnitude variation · Principal stress rotation · Hollow cylinder apparatus · Stress path · Stress orientation

List of Symbols

F, M_t, P_e, P_i	Vertical load, torque, external radial pressure, and internal radial pressure on HCA specimen	R_i	Internal specimen radii
$\tilde{\sigma}_z, \tilde{\sigma}_r, \tilde{\sigma}_\theta, \tilde{\tau}_{z\theta}$	Vertical stress, radial stress, circumferential stress, and shear stress in HCA specimen	σ'_z	Principal stress corresponding to the vertical stress
$\sigma_z, \sigma_r, \sigma_\theta, \tau_{z\theta}$	Average vertical stress, radial stress, circumferential stress, and shear stress in a continuum	σ'_θ	Principal stress corresponding to the circumferential stress
R_e	External specimen radii	α	Rotation angle of the major principal stress axis
		$\sigma_{13}, \sigma_{31}, \tau_{13}, \tau_{31}$	Opposite normal stresses and shear stresses in Mohr circle
		$\sigma_1, \sigma_2, \sigma_3$	Major, intermediate, and minor principal stresses
		δ	Rotation angle between σ_1 and σ_{13} in Mohr circle
		θ_σ	Lode angle
		σ_{ij}	Cauchy stress tensor
		S_{ij}	Stress deviator tensor
		S_1, S_2, S_3	Major, intermediate, and minor principal stress deviators
		J_2	Second deviatoric stress invariant
		p	Hydrostatic pressure
		b	Intermediate principal stress coefficient
		q	Equivalent shear stress

✉ Zhen Li
zhenli.james@qq.com

✉ Hui Zhou
hzhou@whrsm.ac.cn

¹ International Joint Research Laboratory of Henan Province for Underground Space Development and Disaster Prevention, School of Civil Engineering, Henan Polytechnic University, Jiaozuo 454000, Henan, China

² State Key Laboratory of Geomechanics and Geotechnical Engineering, Institute of Rock and Soil Mechanics, Chinese Academy of Sciences, Wuhan 430071, Hubei, China

α	Rotation rate of the major principal stress axis
R	The downward thrust of piston rod produced by oil pressure

1 Introduction

Geomaterial behavior is influenced by factors such as stress path, anisotropy, and type of loading (Lee et al. 1999). Any theoretical model for predicting the performance of engineering structures must consider these factors. Among the factors, the stress path is widely considered suitable for evaluating the safety of engineering construction. Practically, the change in the stress state is represented by principal stress magnitude variation (PSMV) and principal stress rotation (PSR). The PSMV effect has been fully investigated in previous works. Before tunnel construction, there is an equilibrium between the space ahead of the tunnel face and the surrounding ground. Early research showed that the excavation leads to discontinuous distribution of engineering structure, accompanied by the change in the value of radial stress and tangential stress (Fenner 1938). Several types of experiments have been performed to study the stress–strain behavior of the representative element under the PSMV effect. These include the triaxial test (Ding et al. 2016) and true triaxial test (Feng et al. 2016; He et al. 2010). In these tests, the magnitude of the principal stress changes to simulate similar stress paths in engineering projects.

To facilitate more generalized stress-path testing of soils, such as PSR testing, the more sophisticated hollow cylinder apparatus (HCA) was developed for use in soils. HCAs allow independent control of the magnitude of the three principal stresses and rotation of the principal stress axes. Hight et al. (1983) described both the design and principles of operation of a new HCA and its use in the investigation of PSR effects in sands and clays. Saada et al. (1983) introduced a thin hollow cylinder used in the soil laboratory for studies of soil strength and stability under both static and earthquake conditions. Vaid et al. (1990) used a new HCA to study the loose and dense sand behavior and assessed the stress nonuniformity across the wall of the specimen. Talesnick et al. (2000) determined five mechanical parameters with HCA to describe the elastic behavior of a transverse isotropic rock. O’Kelly and Naughton (2005) introduced a new and automated HCA and studied the stress–strain responses of Leighton Buzzard sand over the intermediate to failure strain range.

Although such soil apparatuses are still rare, their development and use have steadily increased. However, HCAs used in rocks are quite limited. Lee et al. (2002) used HCA to analyze the yield surface of Mu-San sandstone under a true triaxial stress path. Alsayed (2002) used the Hoek

triaxial cell and hollow cylinder sandstone to conduct a series of triaxial and polyaxial compression tests. Yang (2016) investigated the deformation, peak strength, and crack damage behavior of hollow sandstone specimens under different confining pressures with various hole diameters. Based on the horizontal and vertical cross-sectional CT images, Yang (2018) evaluated the internal damage behavior of hollow-cylinder sandstone specimens under confining pressures. Although existing studies have attempted to use a hollow cylinder specimen in rocks, the test regarding the PSR effect has never been investigated. Alsayed (2002) found that the lack of suitable testing facilities and the cost and effort required for developing such facilities may have caused some hindrances. Recently, Zhou et al. (2018) successfully developed a new rock mechanical experimental technique and device, and firstly reported a simultaneous control of both stress magnitude variation and orientation in rock test. However, the methodology for establishing a generalized stress path with a versatile HCA taking into account the PSMV and PSR effects in rock mechanics has never been systematically studied.

In this paper, the stress paths used to simulate the PSMV and PSR and its methodology were systematically investigated. The equivalent stresses in the element representing the HCA sample and its role on the PSMV and PSR were studied. The orientation angle of major principal stress was defined in an alternative prospect. Additionally, the variations in stresses associated with the complex stress path were derived in detail. Our methodology contributes to the HCA development and engineering simulation in rock mechanics.

2 Motivation of Hollow Cylinder Test and Stress Path Design

PSR is a common stress path in geotechnical engineering, and it can be induced by dynamic loading events such as earthquakes, vehicular traffic, tunnel excavation, and ocean waves. After the rotation of the principal stress axes was proposed, more emphasis has been placed on the effect of PSR in soil tests and theories. Wang et al. (2016) took into account the impact of PSR under earthquake loading using an elastoplastic soil model. Lin et al. (2016) carried out a series of cyclic principal stress rotation tests and SEM techniques on intact clay to model the influence of traffic loading. Ishihara and Towhata (1983) explored the nature of cyclic loading in seabed soil deposits due to travelling waves. Most studies assessed the theoretical model approach using PSR. Furthermore, Yang and Yu (2013) used a typical and representative kinematic hardening soil model to reproduce soil responses under PSR. Gutierrez et al. (2009) developed a constitutive model for the behavior of sands during monotonic simple shear loading. Nishimura and Towhata

(2004) proposed a three-dimensional stress–strain model of sand using the concept of multiple shear mechanisms.

There is no suitable test equipment with completing PSR effect for rock, so the research is limited to numerical simulation and theoretical analysis in rocks. Eberhardt (2001) explored near-field stress paths during the progressive advancement of a tunnel face using a three-dimensional finite-element approach, and proposed that the three-dimensional stress field encompasses a series of deviatoric stress and also increases or decreases across several rotations of the principal stress axes. Diederichs et al. (2004) performed a case study illustrating the influence of tunnel-induced stress rotation on crack propagation, interaction, and ultimately coalescence and failure. Zhou (2010) developed a micro-mechanics-based model to investigate microcrack damage mechanism of four stages of brittle rock under PSR. Lastly, Zhang et al. (2011) used the simulation methods of micro-mechanics and the 3D simulation of the excavation process

to study the effect of PSR on layered fractures at the Jinping II Hydropower Station. For tunneling excavation, a spatial stress redistribution accompanied by deformation occurs around the working face (Cantieni and Anagnostou 2009). Here we summarized the evolution of principal stresses at tunnel roof during tunneling excavation in Fig. 1. As the tunnel face approaches and passes through a unit volume of surrounding rock, the spatial evolution of the stress field encompasses a series of PSMV as well as PSR.

From fracture mechanics for a single crack, wing crack initiates along principal stress direction at crack tip. The propagation of wing crack is restricted because of the influence of other principal stresses on the crack at the vertical direction. After the rotation of principal stress axis, the crack propagates along the direction of new principal stress and the depth of crack propagation increases. For the fracture network (see Fig. 2), when the principal stress reaches the threshold of yield strength, the micro-fractures

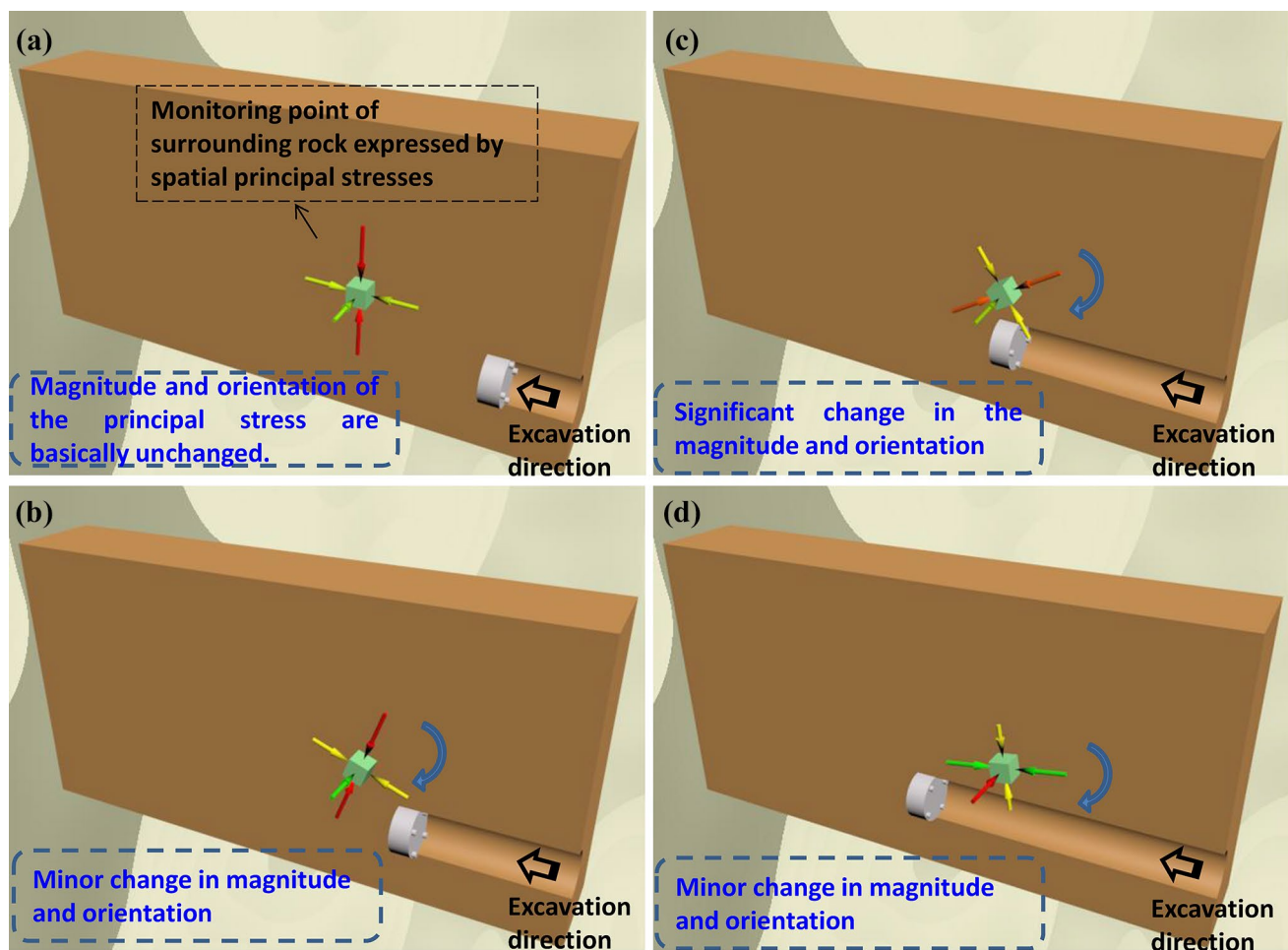


Fig. 1 Evolution of principal stresses at tunnel roof during excavation: **a** Monitoring point is far away from the tunnel face, and basically undisturbed. **b** Monitoring point is getting closer to the tunnel face, and minor change in magnitude and orientation takes place. **c**

Monitoring point is at the position of the tunnel face, and significant change in magnitude and orientation occurs. **d** Monitoring point is gradually away from the tunnel face, and minor change in magnitude and orientation takes place

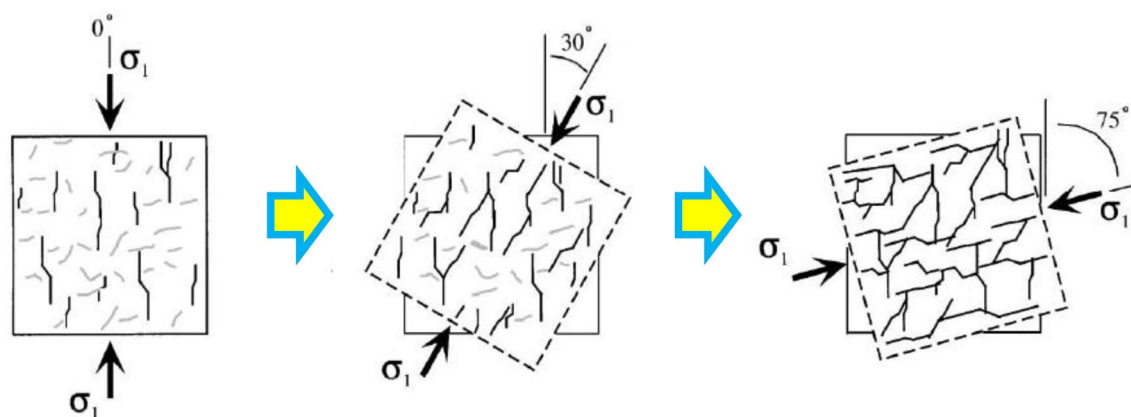


Fig. 2 Conceptual model of damaged fracture network due to rotation of the principal stress axis over a successive series of critical angles (Eberhardt 2001)

mainly extend along the principal stress direction. With the rotation of the principal stress axis, the crack propagation turns to the new principal stress direction. The density of fractures increases and eventually leads to the intersection and penetration of new and old fissures, and the degree of destruction intensifies. It can be seen that compared with the non-rotation of principal stress axis, the failure characteristics of rock after rotation of principal stress axis are significantly changed, and the cracks are further penetrated during rotation.

From above analysis, both of PSMV and PSR play an important role in geotechnical engineering safety and mechanical properties. In fact, conventional geotechnical tests cannot take into account the PSR effect. Other than the hollow cylinder apparatus that works for it, nothing else has been reported. The hollow cylinder tests for soils have been successfully used to study the influence of the PSR effect on the strength and deformation behaviors of soils (Hight et al. 1983; Ishihara and Towhata 1983; Vaid et al. 1990; Sayao and Vaid 1991; O’Kelly and Naughton 2005), and it was demonstrated that strength and deformation parameters of soil are significantly stress-path dependent. However, almost all the traditional mechanical test techniques and devices in the field of rock mechanics can only control the stress magnitude variation, while the simultaneous control of both stress magnitude variation and orientation is actually impossible (Bieniawski 1967; Eberhardt et al. 1999; Ganne and Vervoort 2006; Amann et al. 2011, 2012). Thus, Zhou et al. (2018) developed a new rock experimental technique and device, which can take a simultaneous control of both stress magnitude variation and orientation in rock test.

Corresponding to the newly developed rock hollow cylinder apparatus, the stress path suitable for the test instrument should be developed. Table 1 lists the stress paths commonly used in the existing HCA tests for reference. It can be seen that most of these stress paths were not expressed in the form

of stress invariants. Similarly, in the true triaxial test, most stress paths have not taken the form of stress invariants. The common stress path was criticized by Ma et al. (2017) that all three principal stress invariants, mean stress, octahedral shear stress, and Lode angle, change throughout the test. Consequently, an alternative stress path is desired to isolate the effects of stress invariants relative to the new HCA tests.

3 Principle of Hollow Cylinder Test

3.1 Test Setup and Theories

The hollow cylinder sample was used in the laboratory test. In soil tests, the selection of sample size mainly considers the following factors: (1) the stress and strain distribution is not uniform along the wall thickness due to the specimen curvature. The appropriate size should be chosen to reduce the nonuniformities of stress and strain distribution as much as possible. (2) Reduce the influence of the end effect on the representative element of the specimen. (3) There are enough soil particles along the wall-thickness direction. The wall thickness should be more than ten times of the particle size of the soil. Taking into account the above factors, Hight et al. (1983) defined the nonuniformity coefficient for each individual stress component. Sayao and Vaid (1991) recommended dimensions for HCA specimens: (1) wall thickness is 20–26 mm; (2) $0.65 \leq R_i/R_e \leq 0.82$; (3) the ratio of height to $2R_e$ is 1.8:2.2. Different from soil samples, the rock samples can be prepared by drilling core method, and the relevant experience can ensure the success of the sample preparation. The size of rock hollow cylinder specimen should be based on the principle of thin wall cylinder and minimum end effect. In this HCA test, a hollow cylinder specimen with the outer diameter of 50 mm, inner diameter of 30 mm, and height of 120 mm was selected. To prepare the hollow cylinder specimen more

Table 1 Commonly used stress paths in the existing HCA tests

References of researches	Details in the stress paths
Hight et al. (1983), Sivathayalan and Vaid (2002), O’Kelly and Naughton (2005), Kong et al. (2015), Lin et al. (2016)	The stress paths consisted of major-minor principal stress ratios σ_1/σ_3 , hydrostatic pressure p , intermediate principal stress coefficient b and rotation angle of the major principal stress axis α . Common loading: (1) σ_1/σ_3 , p and b remained constant, while α changed. (2) p , b , and α remained constant, while σ_1/σ_3 changed
O’Kelly and Naughton (2009)	σ_1/σ_3 changed, while p and α were held constant. $b=0$ or increased from 1 to 0.5
Jiang et al. (2013)	The stress paths consisted of $(\sigma_1 - \sigma_3)/p$, p , b and α . Loading: (1) $(\sigma_1 - \sigma_3)/p$ and p remained constant while the value of b was 0.2, 0.5, and 0.9, respectively, during the rotation of principal stress axis. (2) p and b unchanged, $(\sigma_1 - \sigma_3)/p$ was varied when principal stress axis rotated. (3) $(\sigma_1 - \sigma_3)/p$ and b constant, while principal stress axis rotated for various p
Miura et al. (1986)	p , b , and $(\sigma_1 - \sigma_3)/(\sigma_1 + \sigma_3)$ constant, when principal stress axis rotated
Vaid et al. (1990)	Principal stress magnitude was constant when principal stress axis rotated, and b was held 0.5
Yang (2016)	P_i was 0, and P_e was constant when σ_z increased until the sample failed
Alsayed (2002)	P_i and P_e were held constant of different values, when σ_z increased until the sample failed
Lee et al. (1999)	Loading path was expressed by p and q , but θ_σ was expressed by functions of α
Predan et al. (2013)	Pure torsion

precisely and efficiently, a double-drill device was developed as shown in Fig. 3. As an alternative method, the samples can also be prepared by drilling the inner hole first and then the outer hole. If the influence of initial anisotropy on mechanical properties needs to be studied, the core can be drilled at different angles along the bedding planes. After the specimen was made, the inner wall was then coated with epoxy sealant, and both ends were bonded with the top cap and base pedestal using the adhesive, respectively, which was implemented with the assistance of a self-developed tooling device in this work. The outer wall was wrapped with a thermoplastic tube and sealed with epoxy sealant at both ends. Through these series of preparation, the internal and external surfaces of the specimen can withstand the confining pressure, and the two ends of the specimen can hold a torque. The whole system is schematized in Fig. 4.

Similar to conventional rock mechanical tests, in this study stress analysis was performed in an element in the middle of specimen vertical wall. The four types of surface traction, namely, vertical load F , torque M_t , external radial pressures P_e , and internal radial pressures P_i , respectively, acting on the hollow cylinder specimen are illustrated in Fig. 5a. These forces induce vertical stress $\tilde{\sigma}_z$, radial stress $\tilde{\sigma}_r$, circumferential stress $\tilde{\sigma}_\theta$, and shear stress $\tilde{\tau}_{z\theta}$ in the wall of the specimen. Referring to the study by Hight et al. (1983), distributions of these stresses are influenced by the curvature and end restraint, but they are basically similar for elastic and plastic materials. For simplicity, the linear elasticity theory was used in analysis. Therefore, $\tilde{\sigma}_r$ and $\tilde{\sigma}_\theta$ are expressed as follows:

$$\tilde{\sigma}_r = \frac{P_e R_e^2 - P_i R_i^2}{R_e^2 - R_i^2} - \frac{(P_e - P_i) R_e^2 R_i^2}{r^2 (R_e^2 - R_i^2)} \tag{1}$$

$$\tilde{\sigma}_\theta = \frac{P_e R_e^2 - P_i R_i^2}{R_e^2 - R_i^2} + \frac{(P_e - P_i) R_e^2 R_i^2}{r^2 (R_e^2 - R_i^2)} \tag{2}$$

in which R_e and R_i are, respectively, the external and internal specimen radii. r is the radius of any point in a hollow cylinder.

To simulate complex stress paths using hollow cylinder apparatus, the thin-wall approach was adopted in preparing specimen. Vaid et al. (1990) proposed that the uniform stress distribution assumption can be used across the wall of the specimen when its dimensions satisfy the conditions to decrease the effect of the curvature and restraint at its end. In this case, the average radial stress σ_r and circumferential stress σ_θ are obtained by averaging data collected across the wall, as follows:

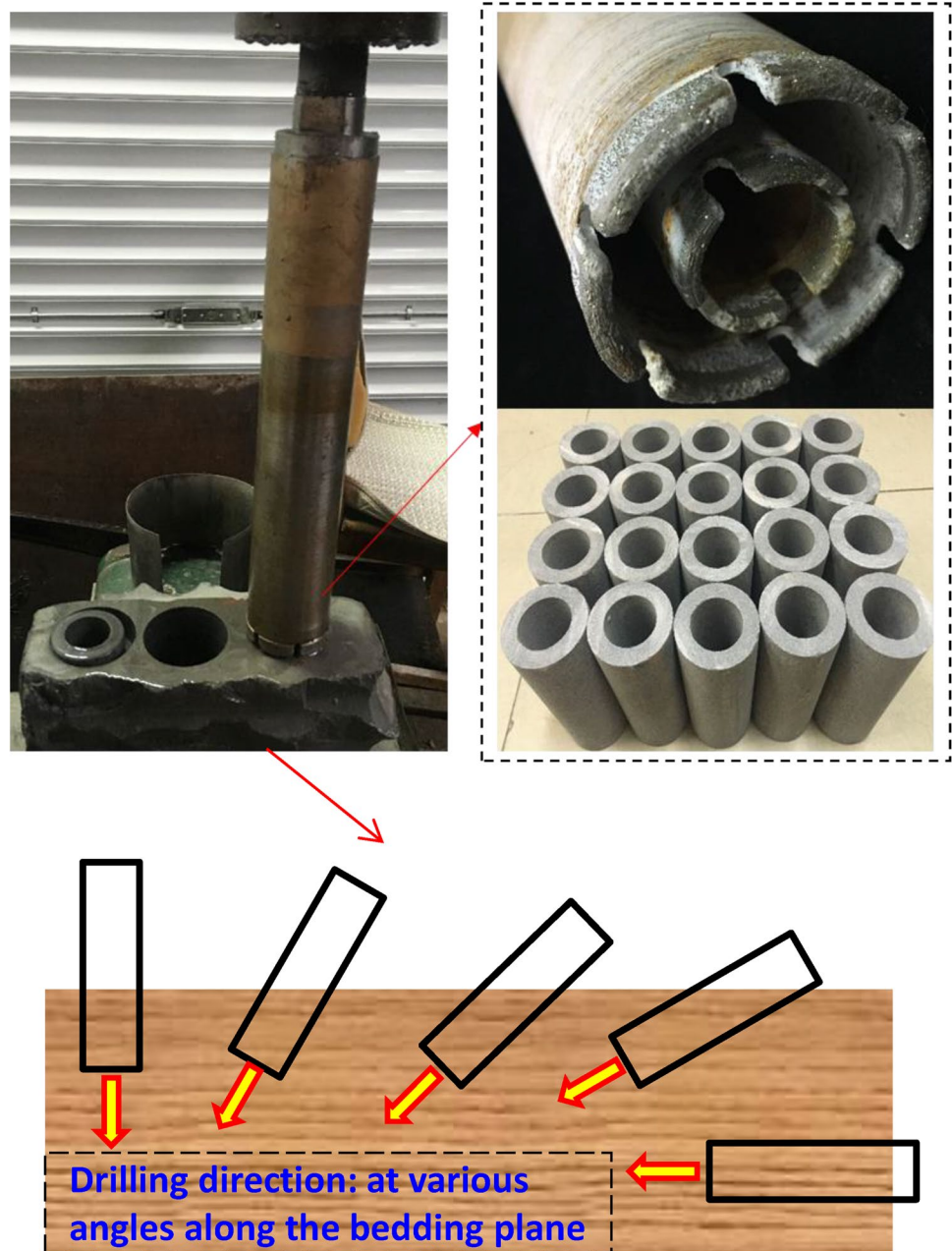
$$\sigma_r = \frac{\int_{R_i}^{R_e} \tilde{\sigma}_r dr}{\int_{R_i}^{R_e} dr} = \frac{P_e R_e + P_i R_i}{R_e + R_i} \tag{3}$$

$$\sigma_\theta = \frac{\int_{R_i}^{R_e} \tilde{\sigma}_\theta dr}{\int_{R_i}^{R_e} dr} = \frac{P_e R_e - P_i R_i}{R_e - R_i} \tag{4}$$

From moment equilibrium and uniform stress distribution assumption, average shear stress $\tau_{z\theta}$ is expressed as follows:

$$\tau_{z\theta} = \frac{3M_t}{2\pi (R_e^3 - R_i^3)} \tag{5}$$

Fig. 3 Sample preparation with drilling device and technique



For axisymmetric material and uniform vertical load, the vertical stress is not dependent on the material constitutive law, and is found only by equilibrium considerations as the following expression

$$\sigma_z = \frac{F + \pi(P_e R_e^2 - P_i R_i^2)}{\pi(R_e^2 - R_i^2)} \quad (6)$$

As shown in Fig. 5a, σ_r is one principal stress. The other two principal stresses, σ'_z and σ'_θ , depend on σ_z , σ_θ , and $\tau_{z\theta}$ in the 2-D stress plane. Without $\tau_{z\theta}$, the

orientations of the principal stresses coincide with the coordinates z and θ . The 2-D element and Mohr circle representation of stress are shown in Fig. 5b, c. The 2-D element after $\tau_{z\theta}$ starts to exist is shown in Fig. 5d. The corresponding Mohr circle is represented in Fig. 5e. The radius of the Mohr circle increases, which means the principal stresses increase. Furthermore, the stress point representing the stress state goes beyond coordinate σ , suggesting that the principal stresses rotate. In this way, the combination of the four stresses with hollow cylinder test would fulfill the loading capacity of PSMV and PSR.

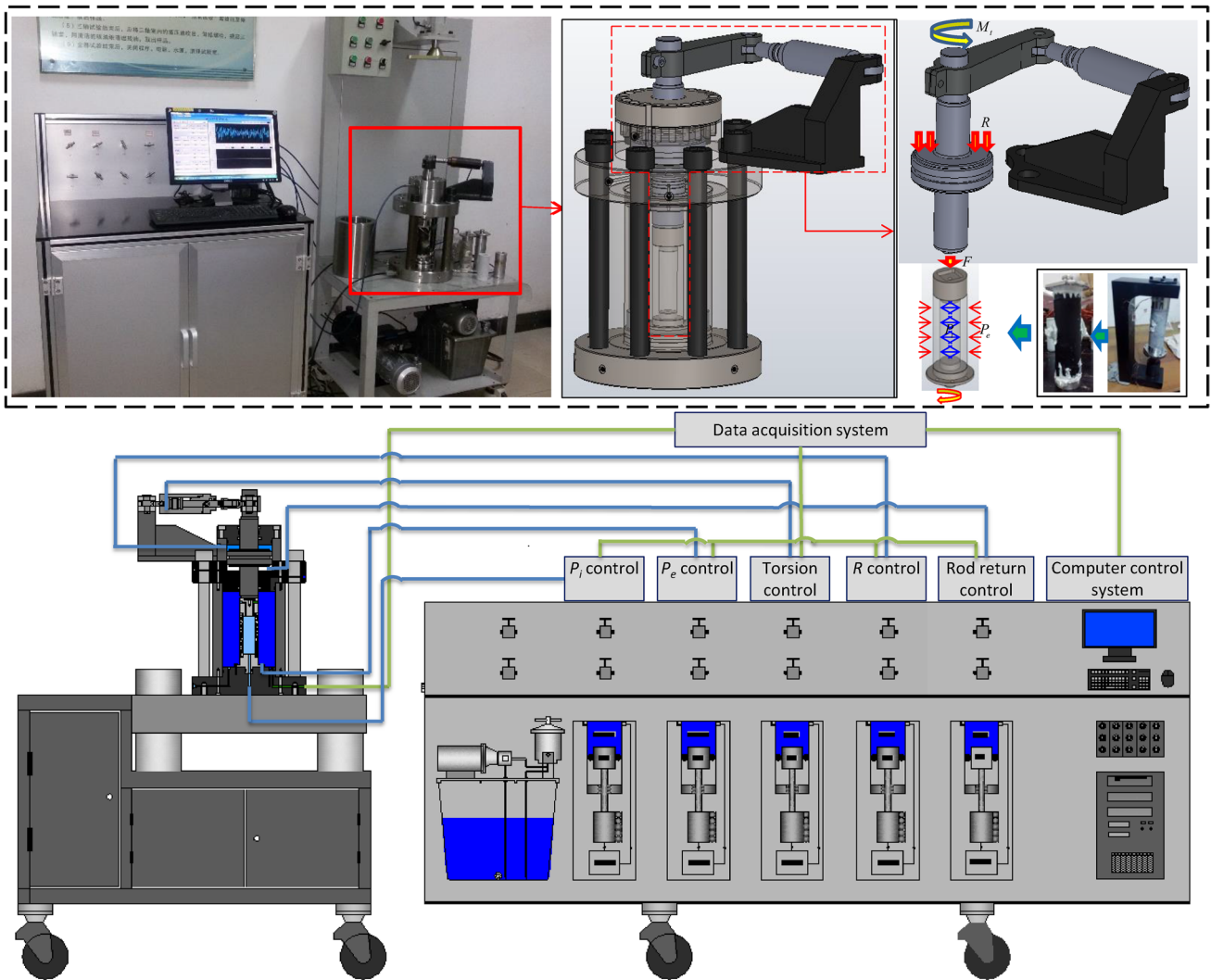


Fig. 4 Schematic of HCA system for rock

3.2 Orientation of the Major Principal Stress

The orientation of the major principal stress is defined as the angle α rotated clockwise from the positive direction of the coordinate z to the major principal stress, as shown in Fig. 6. α ranges from 0 to π .

The radial stress σ_r is considered the intermediate principal stress in the element of the hollow cylinder specimen. The principal element, subjected to principal stresses, rotates in the vertical plane of σ_r , and α has no connection to the radial stress σ_r . Analysis of the 2-D element under the major principal stress and the minimum principal stress is shown in Fig. 7a. Throughout this paper, normal stresses are considered positive when they are compressive, and negative when they are tensile. Shear stresses are viewed positive when the element is rotated counterclockwise.

The plane ef in Fig. 7a divides the element into two parts. Block aef is here analyzed. It is subjected to four stresses: normal stress σ_{13} and shear stress τ_{13} on plane ef , σ_1 on plane ae , and σ_3 on plane af . δ is the angle with positive value rotating counterclockwise from the major principal stress σ_1 to the normal stress σ_{13} , and negative for clockwise rotation. δ ranges from $-\pi/4$ to $\pi/4$. If the area of the plane ef is assumed to be dA , then the areas of planes af and ae are $dA \sin \delta$ and $dA \cos \delta$, respectively. In block aef , the equilibrium equations can be derived as follows:

$$\sigma_{13} \sin \delta - \sigma_3 \sin \delta - \tau_{13} \cos \delta = 0 \tag{7}$$

$$\sigma_1 \cos \delta - \sigma_{13} \cos \delta - \tau_{13} \sin \delta = 0 \tag{8}$$

From Eqs. (7) and (8), the stresses in Mohr circle are expressed as follows:

Fig. 5 Stress conditions in a hollow cylinder element: **a** hollow cylinder sample and stresses on an element in the wall. **b** An element in the z - θ plane without $\tau_{z\theta}$. **c** Mohr circle representation of stress state before loading $\tau_{z\theta}$. **d** An element in the z - θ plane considering $\tau_{z\theta}$. **e** Mohr circle representation of stress state after loading $\tau_{z\theta}$

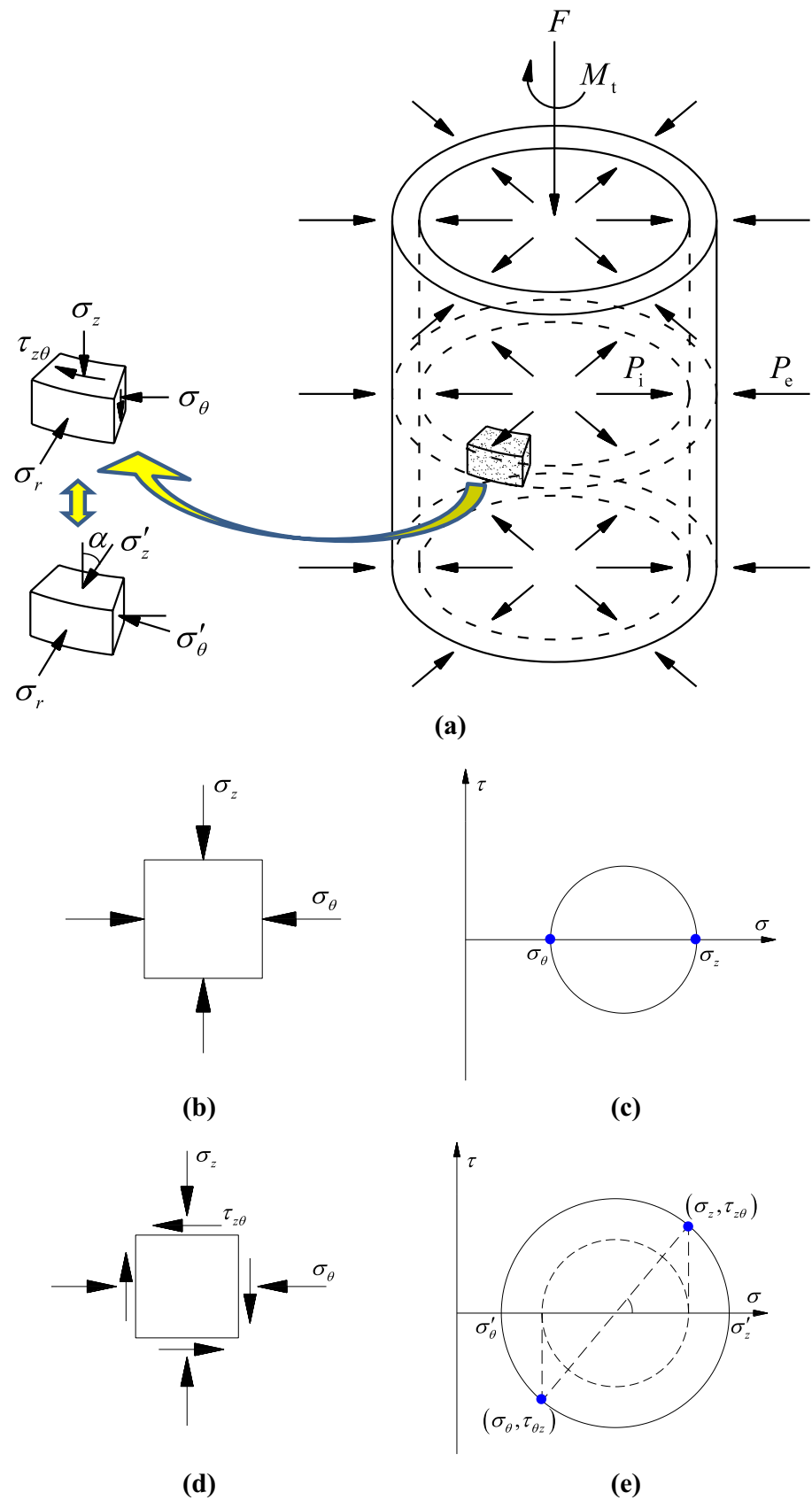
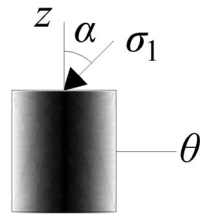


Fig. 6 Illustration of α



$$\sigma_{13} = \frac{\sigma_1 + \sigma_3}{2} + \frac{\sigma_1 - \sigma_3}{2} \cos 2\delta \tag{9}$$

$$\tau_{13} = \frac{\sigma_1 - \sigma_3}{2} \sin 2\delta \tag{10}$$

For $\delta \in [-\pi/4 \text{ to } \pi/4]$, the stress state of σ_{13} and τ_{13} can be represented by the semicircle in Fig. 7b. The following conclusions can be inferred: (a) if normal stress σ_{13} rotates counterclockwise with the angle $|\delta|$ until aligning with direction of the major principal stress σ_1 , and then the shear stress $\tau_{13} < 0$; (b) if normal stress σ_{13} rotates clockwise with the angle δ until it aligns with major principal stress σ_1 , then the shear stress $\tau_{13} > 0$.

According to Fig. 7, the expression of δ is derived as follows:

$$\delta = \frac{1}{2} \arctan [2\tau_{13} / (\sigma_1 - \sigma_3)] \tag{11}$$

In a hollow cylinder element, Eq. (11) could be rewritten as follows:

$$\begin{cases} \delta = \frac{1}{2} \arctan [2\tau_{z\theta} / (\sigma_z - \sigma_\theta)] , \sigma_z > \sigma_\theta \\ \delta = \frac{1}{2} \arctan [2\tau_{\theta z} / (\sigma_\theta - \sigma_z)] , \sigma_z < \sigma_\theta \end{cases} \tag{12}$$

$\tau_{z\theta}$ represents the negative ratio of $\tau_{\theta z}$, which gives a generalized expression of δ as follows:

$$\delta = \frac{1}{2} \arctan [2\tau_{z\theta} / (\sigma_z - \sigma_\theta)] \tag{13}$$

Therefore, based on the Mohr circle theory and limit equilibrium analysis method, δ is derived as Eq. (13) using the stresses consistent with hollow cylinder test. Further conclusions of the element rotation in Fig. 5 can be drawn by the inferences which we have made with Fig. 7b: (a) For the case $\sigma_z > \sigma_\theta$, σ'_z is the major principal stress and σ'_θ is the minimum principal stress (Fig. 8a). When $\tau_{z\theta} < 0$, the element rotates counterclockwise by the angle of $|\delta|$, and σ_z becomes σ'_z . When $\tau_{z\theta} > 0$, the element rotates clockwise by the angle of δ , and σ_z becomes σ'_z . (b) For the case $\sigma_z < \sigma_\theta$, σ'_z is the major principal stress and σ'_θ is the minimum principal stress (Fig. 8b). When $\tau_{\theta z} < 0$, the element rotates counterclockwise by the angle of $|\delta|$, and σ_θ becomes σ'_θ . When $\tau_{\theta z} > 0$, the element rotates clockwise by the angle of δ , and σ_θ becomes σ'_θ .

From conclusions in Fig. 7, we can see that by controlling the magnitudes and directions of normal stress and shear stress, the corresponding principal element can be found by rotation of any plane element at a certain angle of δ . However, this angle is limited to $-\pi/4$ to $\pi/4$ in its definition. If the rotation angle of the major principal stress axis (α) in Fig. 6 is introduced, a more general theory of element rotation in hollow cylindrical test can be established.

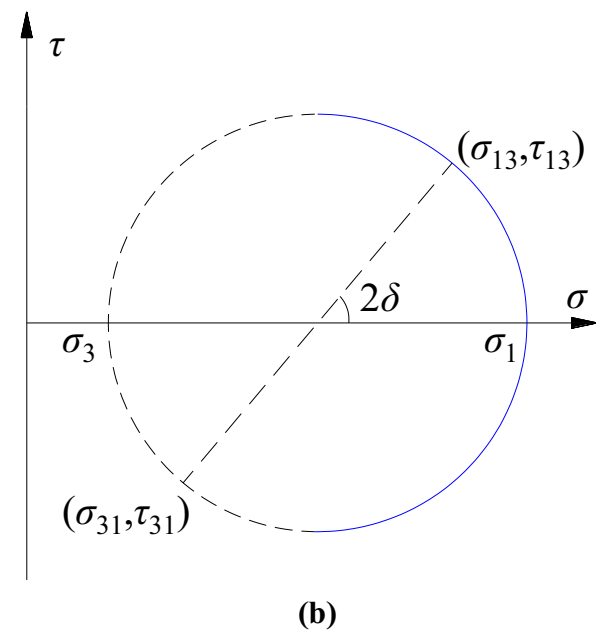
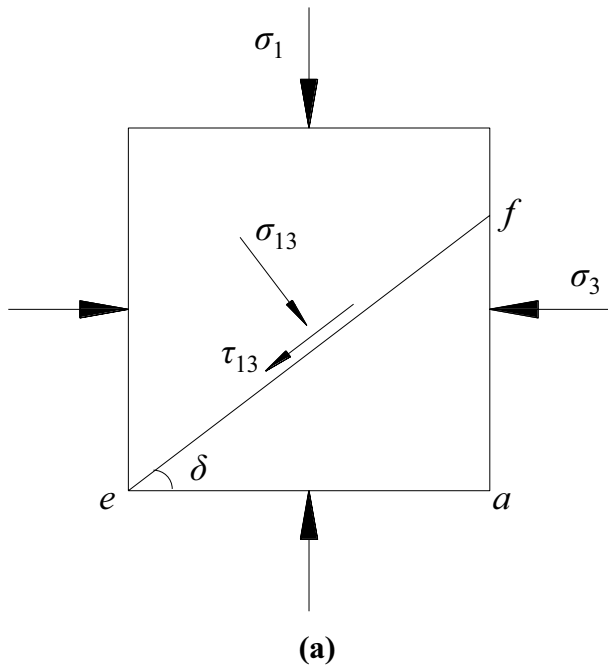


Fig. 7 Description of the link between principal stresses and plane stresses using two kinds of stress state representation: **a** 2-D element with an oblique section. **b** Mohr circle diagram with a semicircle for $\delta \in [-\pi/4 \text{ to } \pi/4]$

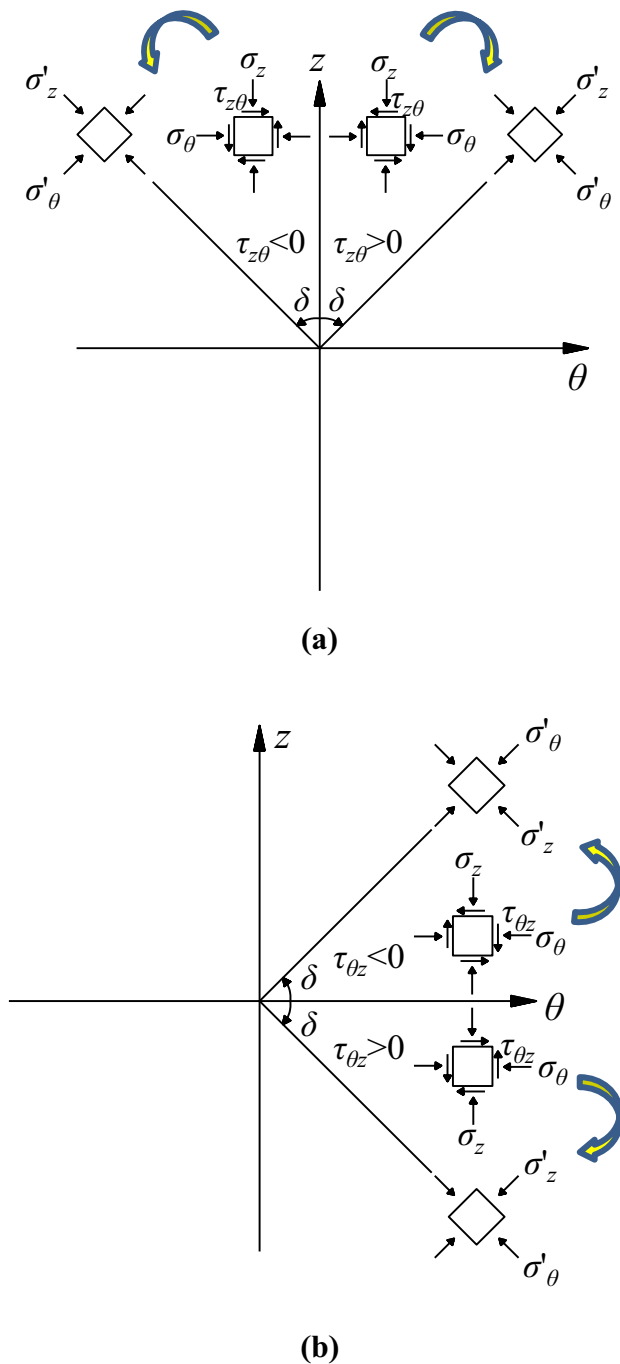


Fig. 8 Identification of the principal element with no shear stresses: **a** case of $\sigma_z > \sigma_\theta$, **b** case of $\sigma_z < \sigma_\theta$

The magnitude of δ is related to $2\tau_{z\theta}$ and $(\sigma_z - \sigma_\theta)$ according to Eq. (13). In this way, depictions of PSR in the $2\tau_{z\theta} - (\sigma_z - \sigma_\theta)$ coordinate system can be sketched as shown in Fig. 9. Figure 9a, b show identification of the principal stress using the angle of δ and α , respectively. For the convenience of analysis, we take the stress point representing the initial stress state of the element in the positive $(\sigma_z - \sigma_\theta)$ coordinate. The stress point then passes through the first quadrant, the positive

$\tau_{z\theta}$ coordinate, the second quadrant, the negative $(\sigma_z - \sigma_\theta)$ coordinate, the third quadrant, the negative $\tau_{z\theta}$ coordinate, the fourth quadrant in turn. For ease of understanding, the stress path is represented in Fig. 9 by the arrow and alphabetical order (a)–(h). In the diagram, we no longer use the element in a general stress state, but we use the principal element for representation. With the stress point changing in turn, the principal element rotates. Based on the above theoretical analysis, Table 2 complements Fig. 9 and shows the plane elements, principal elements and the expression of δ and α in various stress point location in alphabetical order in Fig. 9.

Combining Table 2 and Fig. 9, the stresses and angles of the element during rotation were analyzed with examples. Firstly, the stress point representing the initial stress state of the element is located at the positive $(\sigma_z - \sigma_\theta)$ coordinate, which suggests $\sigma_z > \sigma_\theta$, then σ_z is the major principal stress σ_1 , and σ_θ is the minimum principal stress σ_3 . The corresponding alphabetic number is (a). In this case, $\delta = 0$ and $\alpha = 0$. After that, the stress point moves to the first quadrant, corresponding to the letter (b). $\sigma_z > \sigma_\theta$ and $\tau_{z\theta} > 0$. By the practice of Fig. 8, we can get that σ_z rotates clockwise by the angle of δ and finds the major principal stress $\sigma_1 = \sigma'_z$. In this case, $\delta = \alpha$ and $\alpha \in (0, \pi/4)$. From Eq. (13), $\alpha = \frac{1}{2} \arctan [2\tau_{z\theta} / (\sigma_z - \sigma_\theta)]$. When the stress point continues to move alphabetically to (c), it is located in the positive $\tau_{z\theta}$ coordinate, which suggests $\tau_{z\theta} > 0$ and $\sigma_z = \sigma_\theta$. This is a bit special for obtaining the value of δ . On one hand, when going from (a) to (c) in alphabetical order, σ_z rotates clockwise by $\pi/4$ and finds the maximum principal stress $\sigma_1 = \sigma'_z$, and $\delta = \pi/4$; On the other hand, if we take the order (e) to (c), that is, in the second quadrant, σ_θ rotates counterclockwise by $\pi/4$ and finds the major principal stress $\sigma_1 = \sigma'_\theta$. In this case, $\delta = -\pi/4$. In any case, both approaches can yield consistent results, i.e., $\alpha = \pi/4$. Referring to the above analysis, the rest of the results are obtained, as shown in Table 2 and Fig. 9, and are therefore not restated.

It is worth noting that Table 2 lists the values of α in each case, and the expression of α can be summarized based on the results of Table 2 as follows:

$$\alpha = \begin{cases} \frac{1}{2} \arctan \frac{2\tau_{z\theta}}{\sigma_z - \sigma_\theta}, & \text{if } \sigma_z > \sigma_\theta \text{ and } \tau_{z\theta} \geq 0 \\ \frac{1}{2} \arctan \frac{2\tau_{z\theta}}{\sigma_z - \sigma_\theta} + \frac{\pi}{2}, & \text{if } \sigma_z < \sigma_\theta \\ \frac{1}{2} \arctan \frac{2\tau_{z\theta}}{\sigma_z - \sigma_\theta} + \pi, & \text{if } \sigma_z > \sigma_\theta \text{ and } \tau_{z\theta} < 0 \\ \frac{\pi}{4}, & \text{if } \sigma_z = \sigma_\theta \text{ and } \tau_{z\theta} > 0 \\ \frac{3\pi}{4}, & \text{if } \sigma_z = \sigma_\theta \text{ and } \tau_{z\theta} < 0 \end{cases} \quad (14)$$

4 Methodology for Stress Path in HCA

4.1 Representation of Stress State

For a given stress state with three principal stresses σ_1 , σ_2 , and σ_3 , there exists a point B in the principal stress space

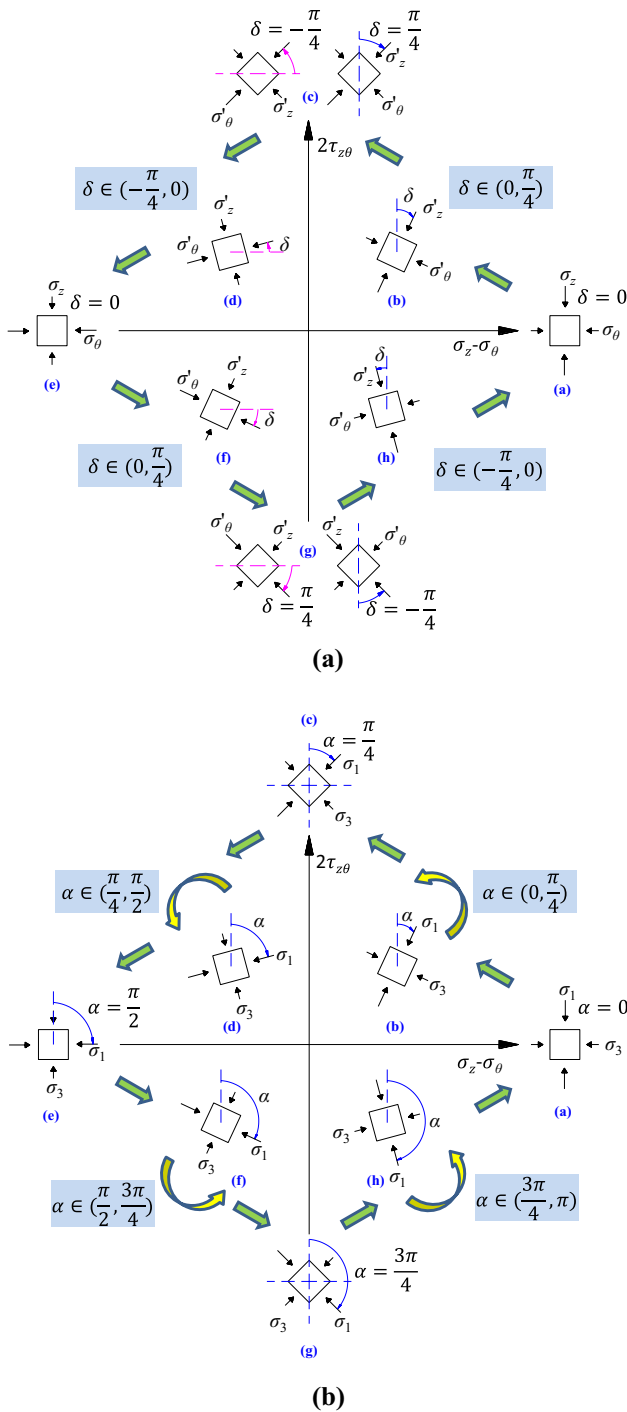


Fig. 9 Mechanism underlying PSR in an element of the hollow cylinder specimen in the $2\tau_{z\theta}$ - $(\sigma_z-\sigma_\theta)$ coordinate system: **a** Identification of the principal stress using the angle of δ . **b** Identification of the principal stress using the angle of α

in Fig. 10a. Vector \overline{OB} may be viewed as the operation of $\overline{OA} + \overline{AB}$. The vector \overline{OA} aligns in the hydrostatic axis. When under hydrostatic pressure, geomaterial, especially rock, is vulnerable to yield. Therefore, the stress path along

the hydrostatic axis is viewed a safe means of loading pressure. On the contrary, the vector \overline{AB} grows longer on the deviatoric plane and becomes limited in the yield envelope. The deviatoric plane is perpendicular to the hydrostatic axis. The stress path deviating from the hydrostatic axis on the deviatoric plane increases the instability of the material. In Fig. 10b, point C is on the yield envelop and defines the boundary of \overline{AB} . Accordingly, the stress tensor σ_{ij} can be decomposed into two parts (Chen and Saleeb 2013) as follows:

$$\sigma_{ij} = p\delta_{ij} + S_{ij} \tag{15}$$

Here, $p\delta_{ij}$ represents the hydrostatic stress tensor. p is hydrostatic pressure defined as $p = \frac{1}{3}\sigma_{kk}$. δ_{ij} is the Kronecker Delta. The value of δ_{ij} gets 1 when $i = j$ and 0 on the contrary. S_{ij} is the stress deviator tensor.

θ_σ is an important parameter in Fig. 10b, representing the following stress relationship:

$$\theta_\sigma = \arctan \frac{2\sigma_2 - \sigma_1 - \sigma_3}{\sqrt{3}(\sigma_1 - \sigma_3)} \tag{16}$$

The length of \overline{AB} equals to $\sqrt{2J_2}$ and J_2 is expressed as $\frac{S_{ij}S_{ij}}{2}$. Thus, the principal stress deviators are as follows:

$$S_1 = \frac{2}{\sqrt{3}}\sqrt{J_2} \cos\left(\theta_\sigma + \frac{\pi}{6}\right) \tag{17}$$

$$S_2 = \frac{2}{\sqrt{3}}\sqrt{J_2} \cos\left(\theta_\sigma - \frac{\pi}{2}\right) \tag{18}$$

$$S_3 = \frac{2}{\sqrt{3}}\sqrt{J_2} \cos\left(\theta_\sigma + \frac{5\pi}{6}\right) \tag{19}$$

As shown in Fig. 10c, q is the equivalent shear stress and $q = \sqrt{3J_2}$. There exists a relationship between the geometric length in Fig. 10a, c, such as $|\overline{OA'}| = 1/\sqrt{3}|\overline{OA}|$ and $|\overline{A'B'}| = \sqrt{3/2}|\overline{AB}|$.

4.2 Hydrostatic Pressure Stress Path

In this case, the stress path represents the line \overline{OA} in the principal stress space, point A on the deviatoric plane, and line $\overline{A'B'}$ on the meridian plane (see Fig. 10). The three principal stresses are equal, as shown by

$$\sigma_z = \sigma_r = \sigma_\theta = p \tag{20}$$

4.3 PSMV Stress Path on the Deviatoric Plane

The PSMV stress path in this section is discussed after the hydrostatic pressure is loaded as p_0 . Presume the vertical

Table 2 Illustrations of the element with the stresses (normal stresses and shear stresses, or principal stresses) and the expression of δ and α for various stress point locations in the $2\tau_{z\theta} - (\sigma_z - \sigma_\theta)$ coordinate system

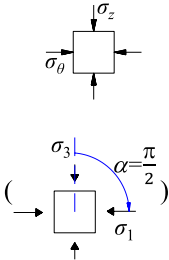
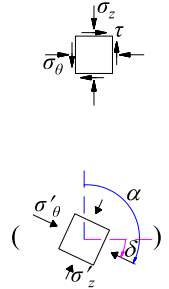
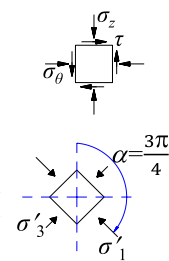
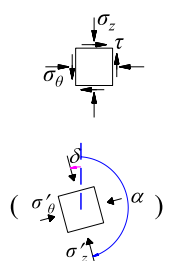
Alphabetical order in Fig.9	Stress point location	Illustration of the stresses	Illustration of the element	Domain of δ	Domain of α	Expression of α
(a)	Positive $(\sigma_z - \sigma_\theta)$ coordinate	$\sigma_z > \sigma_\theta$, $\tau_{z\theta} = 0$		0	0	0
(b)	First quadrant	$\sigma_z > \sigma_\theta$, $\tau_{z\theta} > 0$, $\sigma_1 = \sigma'_z$, $\sigma_3 = \sigma'_\theta$		$(0, \frac{\pi}{4})$	$(0, \frac{\pi}{4})$	$\frac{1}{2} \arctan \frac{2\tau_{z\theta}}{\sigma_z - \sigma_\theta}$
(c)	Positive $2\tau_{z\theta}$ coordinate	$\sigma_z = \sigma_\theta$, $\tau_{z\theta} > 0$		$\frac{\pi}{4}$ for $\sigma_z - \sigma_\theta \rightarrow 0^+$, $-\frac{\pi}{4}$ for $\sigma_z - \sigma_\theta \rightarrow 0^-$	$\frac{\pi}{4}$	$\frac{\pi}{4}$
(d)	Second quadrant	$\sigma_z < \sigma_\theta$, $\tau_{z\theta} < 0$, $\sigma_1 = \sigma'_\theta$, $\sigma_3 = \sigma'_z$		$(-\frac{\pi}{4}, 0)$	$(\frac{\pi}{4}, \frac{\pi}{2})$	$\frac{1}{2} \arctan \frac{2\tau_{z\theta}}{\sigma_z - \sigma_\theta} + \frac{\pi}{2}$

stress σ_z , radial stress σ_r , circumferential stress σ_θ is loaded to $p_0 + \Delta\sigma_z$, $p_0 + \Delta\sigma_r$ and $p_0 + \Delta\sigma_\theta$, respectively. In this case, the rotation angle of the maximum principal stress axis α , the Lode angle θ_σ , and the hydrostatic pressure p are constant. The equivalent shear stress q is loaded until yield. Its stress path can be represented in Fig. 10 as the line **AB** in the principal stress space and **A'B'** on the meridian plane.

To assess the influence of the intermediate principal stress, intermediate principal stress coefficient b is widely used. b has the relationship with θ_σ as follows:

$$\sqrt{3} \tan \theta_\sigma = 2b - 1 \tag{21}$$

Table 2 (continued)

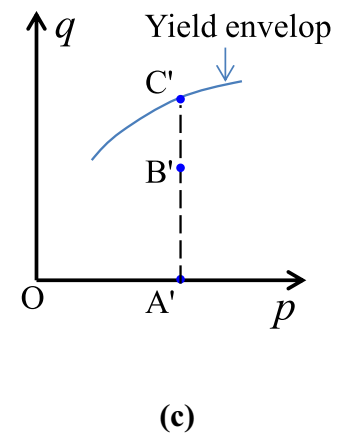
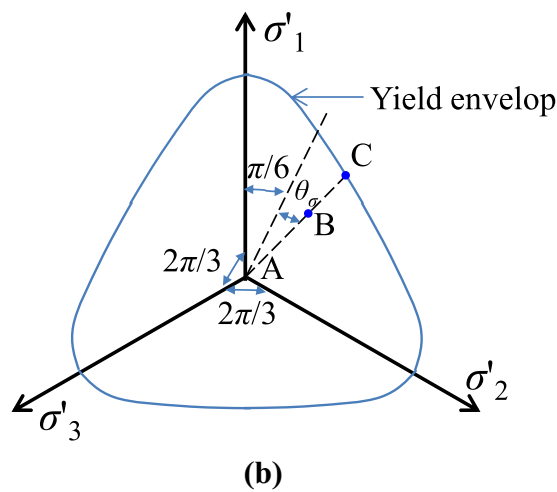
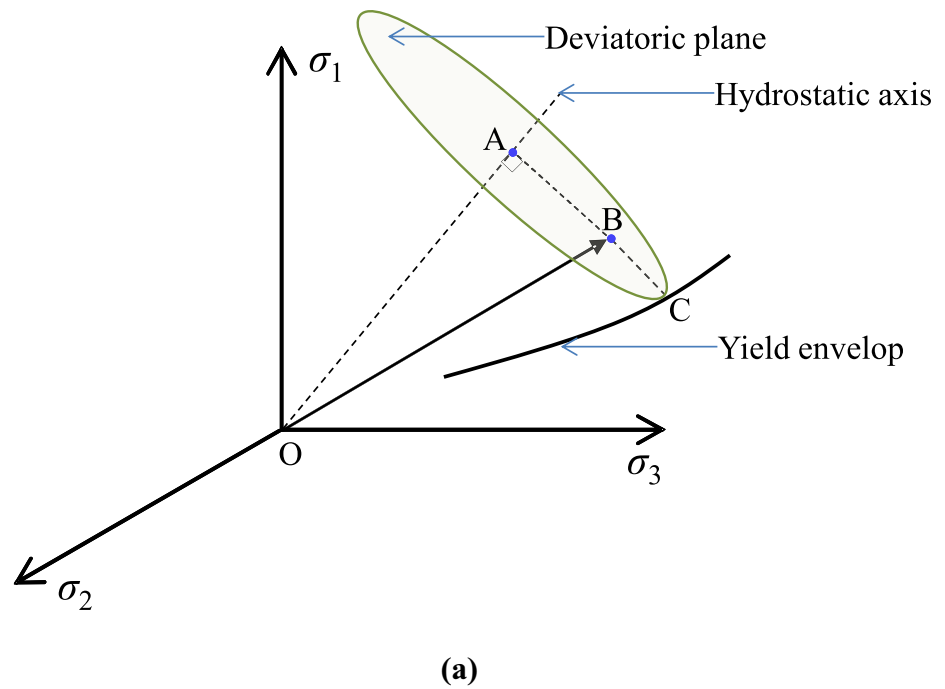
Alphabetical order in Fig.9	Stress point location	Illustration of the stresses	Illustration of the element	Domain of δ	Domain of α	Expression of α
(e)	Negative $(\sigma_z - \sigma_\theta)$ coordinate	$\sigma_z < \sigma_\theta,$ $\tau_{z\theta} = 0$		0	$\frac{\pi}{2}$	$\frac{\pi}{2}$
(f)	Third quadrant	$\sigma_z < \sigma_\theta,$ $\tau_{\theta z} > 0,$ $\sigma_1 = \sigma'_\theta,$ $\sigma_3 = \sigma'_z$		$(0, \frac{\pi}{4})$	$(\frac{\pi}{2}, \frac{3\pi}{4})$	$\frac{1}{2} \arctan \frac{2\tau_{z\theta}}{\sigma_z - \sigma_\theta} + \frac{\pi}{2}$
(g)	Negative $2\tau_{z\theta}$ coordinate	$\sigma_z = \sigma_\theta,$ $\tau_{z\theta} < 0$		$-\frac{\pi}{4}$ for $\sigma_z - \sigma_\theta \rightarrow 0^+,$ $\frac{\pi}{4}$ for $\sigma_z - \sigma_\theta \rightarrow 0^-$	$\frac{3\pi}{4}$	$\frac{3\pi}{4}$
(h)	Fourth quadrant	$\sigma_z > \sigma_\theta,$ $\tau_{z\theta} < 0,$ $\sigma_1 = \sigma'_z,$ $\sigma_3 = \sigma'_\theta$		$(-\frac{\pi}{4}, 0)$	$(\frac{3\pi}{4}, \pi)$	$\frac{1}{2} \arctan \frac{2\tau_{z\theta}}{\sigma_z - \sigma_\theta} + \pi$

Note that the element in parentheses represents the principal element, while the element without parentheses is the plane element subjected to normal stresses and shear stresses

The expression of α and stress state corresponding to the stress point in the $2\tau_{z\theta} - (\sigma_z - \sigma_\theta)$ coordinate system vary at different quadrants and coordinates, as shown in Table 2 and

Eq. (14). The stress path was discussed with the $2\tau_{z\theta} - (\sigma_z - \sigma_\theta)$ coordinate system.

Fig. 10 Description of stress state: **a** stress state representation in the principal stress space. **b** Stress point and yield envelop on the deviatoric plane. **c** Stress point and yield envelop on the meridian plane



If the stress state point is located at the first quadrant, then $\sigma_z > \sigma_r > \sigma_\theta$ and $\tau_{z\theta} > 0$. The major principal stress and minimum principal stress are expressed as follows:

$$\sigma_1 = \frac{\sigma_z + \sigma_\theta}{2} + \sqrt{\frac{(\sigma_z - \sigma_\theta)^2}{4} + \tau_{z\theta}^2} \quad (22)$$

$$\sigma_3 = \frac{\sigma_z + \sigma_\theta}{2} - \sqrt{\frac{(\sigma_z - \sigma_\theta)^2}{4} + \tau_{z\theta}^2} \quad (23)$$

$$b = \frac{\sigma_2 - \sigma_3}{\sigma_1 - \sigma_3} \quad (24)$$

$$\tan 2\alpha = \frac{2\tau_{z\theta}}{\sigma_z - \sigma_\theta} \quad (25)$$

$$p = \sigma_z + \sigma_\theta + \sigma_r = \text{const.} \quad (26)$$

$$q = \sqrt{3J_2} \quad (27)$$

From Eqs. (22) to (27), we have the following:

The independent variables b , α , p , and q in the stress path can be expressed as follows:

$$b = \frac{\Delta\sigma_r - \frac{\Delta\sigma_z + \Delta\sigma_\theta}{2} + \left| \frac{\Delta\sigma_z - \Delta\sigma_\theta}{2 \cos 2\alpha} \right|}{\left| \frac{\Delta\sigma_z - \Delta\sigma_\theta}{\cos 2\alpha} \right|} \tag{28}$$

$$\tan 2\alpha = \frac{2\tau_{z\theta}}{\Delta\sigma_z - \Delta\sigma_\theta} \tag{29}$$

$$\Delta\sigma_z + \Delta\sigma_\theta + \Delta\sigma_r = 0 \tag{30}$$

$$q = \sqrt{\frac{(\Delta\sigma_z - \Delta\sigma_\theta)^2 + (\Delta\sigma_r - \Delta\sigma_\theta)^2 + (\Delta\sigma_z - \Delta\sigma_r)^2}{2} + 3\tau_{z\theta}^2} \tag{31}$$

At the first quadrant $\sigma_z > \sigma_\theta$ and $\cos 2\alpha > 0$, according to Eqs. (28) and (30) we have the following:

$$\Delta\sigma_\theta = \Delta\sigma_r \frac{3 \cos 2\alpha - 1 + 2b}{2(1 - 2b)} \tag{32}$$

$$\Delta\sigma_z = \Delta\sigma_r \frac{-3 \cos 2\alpha - 1 + 2b}{2(1 - 2b)} \tag{33}$$

From Eqs. (29) and (31) through (33), the variable q can be written as follows:

$$q = 3 \left| \frac{\Delta\sigma_r}{1 - 2b} \right| \sqrt{b^2 - b + 1} \tag{34}$$

If $b < 0.5$, according to Eq. (33) $\Delta\sigma_z \Delta\sigma_r < 0$. Otherwise, according to Eq. (32) $\Delta\sigma_\theta \Delta\sigma_r < 0$. Therefore, $\Delta\sigma_r < 0$ for $b < 0.5$ and $\Delta\sigma_r > 0$ for $b > 0.5$. Then Eq. (34) can be rewritten as follows:

$$q = \frac{3\Delta\sigma_r}{2b - 1} \sqrt{b^2 - b + 1} \tag{35}$$

From Eqs. (29), (32), (33), and (35), the four stresses associated with the element in the hollow cylinder can be expressed as follows:

$$\Delta\sigma_z = \frac{3 \cos 2\alpha + 1 - 2b}{6\sqrt{b^2 - b + 1}} q \tag{36}$$

$$\Delta\sigma_r = \frac{2b - 1}{3\sqrt{b^2 - b + 1}} q \tag{37}$$

$$\Delta\sigma_\theta = \frac{-3 \cos 2\alpha + 1 - 2b}{6\sqrt{b^2 - b + 1}} q \tag{38}$$

$$\tau_{z\theta} = \frac{\sin 2\alpha}{2\sqrt{b^2 - b + 1}} q \tag{39}$$

Table 3 Variations in stresses in the PSMV stress path on the deviatoric plane

$\Delta\sigma_z$	$\Delta\sigma_r$	$\Delta\sigma_\theta$	$\tau_{z\theta}$
$\frac{2-b}{3\sqrt{b^2-b+1}}q$	$\frac{2b-1}{3\sqrt{b^2-b+1}}q$	$\frac{-1-b}{3\sqrt{b^2-b+1}}q$	0

Similarly, at the other quadrants, we find the same equations as derived above. In the PSMV stress path, when the hydrostatic pressure is loaded as p_0 , and we can load the variable q until rock yields at the given constants b and $\alpha = 0$. The controlling methodology of PSMV stress path on the deviatoric plane is shown in Table 3.

4.4 PSR Stress Path

The PSR stress path discussed in this section is a sequential load followed by PSMV stress path. Presume that, before PSR stress path, the four stresses in the element are $\sigma_z, \sigma_r, \sigma_\theta$, and $\tau_{z\theta} = 0$. After PSR loading, the stresses change to $\sigma_z + \Delta\sigma_z, \sigma_r + \Delta\sigma_r, \sigma_\theta + \Delta\sigma_\theta$, and $\Delta\tau_{z\theta}$. In this situation, the principal stress magnitude remains constant but the orientation of principal stress axis changes. There is no variation in the intermediate principal stress.

$$\Delta\sigma_r = 0 \tag{40}$$

The hydrostatic pressure remains constant and, according to Eq. (40), we have the following:

$$\Delta\sigma_z + \Delta\sigma_\theta = 0 \tag{41}$$

Based on Eq. (41) and the expression of principal stresses in Eqs. (22) and (23), the validation that no change in the principal stress magnitude can be expressed as follows:

$$\Delta\tau_{z\theta}^2 = \Delta\sigma_\theta(\sigma_z - \sigma_\theta) - \Delta\sigma_\theta^2 \tag{42}$$

Notice that there is a generalized expression as derived from Table 2.

$$\tan 2\alpha = \frac{2\Delta\tau_{z\theta}}{\sigma_z + \Delta\sigma_z - \sigma_\theta - \Delta\sigma_\theta} \tag{43}$$

From Eqs. (41) to (43), we have the following:

$$\left| (\sigma_z - \sigma_\theta) \cos 2\alpha \right| = \left| \sigma_z - \sigma_\theta - 2\Delta\sigma_\theta \right| \tag{44}$$

At the PSMV loading stage before the PSR loading, the direction of the major principal stress α is equal to 0, and $\sigma_z - \sigma_\theta > 0$. Moreover, during the PSR loading process, $\cos 2\alpha (\sigma_z + \Delta\sigma_z - \sigma_\theta - \Delta\sigma_\theta) > 0$. Then Eq. (44) may be rewritten as follows:

$$(\sigma_z - \sigma_\theta) \cos 2\alpha = \sigma_z - \sigma_\theta - 2\Delta\sigma_\theta \tag{45}$$

According to Eqs. (41), (43), and (45), we have the following:

$$\Delta\sigma_\theta = \frac{(\sigma_z - \sigma_\theta)(1 - \cos 2\alpha)}{2} \tag{46}$$

$$\Delta\sigma_z = \frac{(\sigma_z - \sigma_\theta)(\cos 2\alpha - 1)}{2} \tag{47}$$

$$\tau_{z\theta} = \frac{\sin 2\alpha}{2} (\sigma_z - \sigma_\theta) \tag{48}$$

The controlling methodology of PSR stress path is shown in Table 4.

4.5 Complex Stress Path Considering PSMV and PSR Effect

Assume there is no change in α before the discussed complex loading in this section. During the consequent loading process, hydrostatic pressure is kept constant, while the equivalent shear stress q and the orientation of the major principal stress α change. The loading of q and α corresponds to the PSMV and PSR process, respectively. Equations (36) to (39) show how the four stresses in the element change with q and α for a constant p . The controlling methodology of complex stress path considering PSMV and PSR effect is shown in Table 5.

5 Verifications

5.1 PSMV Stress Path

To simulate the PSMV stress path on the deviatoric plane, a numerical experimentation was conducted. First, hydrostatic pressure p was loaded at rate of 1 MPa/s until 30 MPa. Then the equivalent shear stress q was loaded at 1 MPa/s to 40 MPa. During the PSMV loading process, b was set to 0.3.

Table 4 Stresses variations in the PSR stress path

$\Delta\sigma_z$	$\Delta\sigma_r$	$\Delta\sigma_\theta$	$\tau_{z\theta}$
$\frac{(\sigma_z - \sigma_\theta)(\cos 2\alpha - 1)}{2}$	0	$\frac{(\sigma_z - \sigma_\theta)(1 - \cos 2\alpha)}{2}$	$\frac{\sin 2\alpha}{2} (\sigma_z - \sigma_\theta)$

Table 5 Stresses variations in the stress path coupling PSMV and PSR effect

$\Delta\sigma_z$	$\Delta\sigma_r$	$\Delta\sigma_\theta$	$\tau_{z\theta}$
$\frac{3 \cos 2\alpha + 1 - 2b}{6\sqrt{b^2 - b + 1}} q$	$\frac{2b - 1}{3\sqrt{b^2 - b + 1}} q$	$\frac{-3 \cos 2\alpha + 1 - 2b}{6\sqrt{b^2 - b + 1}} q$	$\frac{\sin 2\alpha}{2\sqrt{b^2 - b + 1}} q$

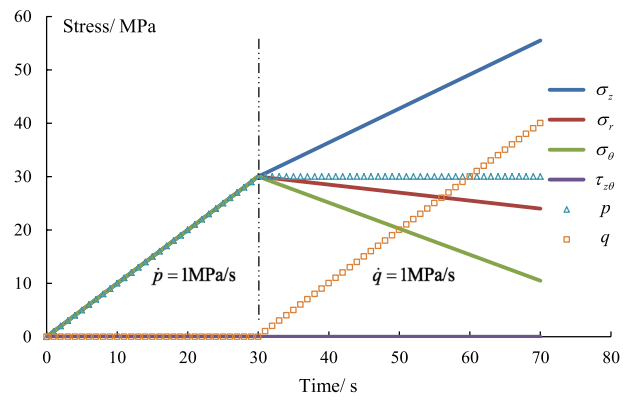


Fig. 11 Variations in the stresses in a PSMV loading simulation

The stresses in the test control are shown in Fig. 11. In this simulation, we see $\tau_{z\theta}$ equals to zero in the whole process, which means the PSR effect does not work. In the hydrostatic pressure loading, q remains zero, while σ_z , σ_r , σ_θ and p rise equally to 30 MPa. Then, σ_z increases, and the other two principal stresses decrease at different rates. p keeps the value of 30 MPa and q increases from zero.

Here we used a test case for verification. Different from the above numerical simulation, in the test, b equals to 0.5, thus θ_σ equals to zero referring to the Eq. (21). The expected stress path is set as shown in Fig. 12a. First, p was applied simultaneously from point O to A, and the stress state was $\sigma_z = \sigma_r = \sigma_\theta = p$ at point A according to the Eq. (20). Then, q was successively applied. From Table 3, $\Delta\sigma_z = \Delta\sigma_\theta$, while σ_r remained constant.

Figure 12b–d showed the load paths, the principal stress paths and the stress invariant path in the test, respectively. During the test, to follow the prescribed stress path precisely, P_e , P_i and F were loaded to 30 MPa in increments. Then, P_e , P_i and F changed the values to make $\Delta\sigma_z = \Delta\sigma_\theta$. In this process, σ_r and p were observed constant. It is worth noting that, the load curves of σ_z and q fluctuated a lot in several segments. This is because in Fig. 4, the force area of R is larger than that of F , which results in the vertical stress σ_z of the sample being about eight times that of the oil pressure at R . So the slight fluctuation of the oil pressure at R can cause the fluctuation of σ_z to be magnified. If the force area of the piston rod at R was similar to the vertical force area of the rock sample, the amplification effect of this fluctuation would be weakened, and the experimental results would be more satisfactory. In brief, through the designed methodology, PSMV effect can be achieved with a reasonable result.

5.2 PSR Stress Path

To exemplify a PSR stress path, a numerical experimentation was conducted as shown in Fig. 13. First, p was loaded at

30 MPa, followed by q at 40 MPa, and b at 0.3. During the PSR loading process, the orientation of the major principal stress axis α rotated at rate of $\pi/400$ per second. The principal stresses remained constant throughout the loading simulation. This process can be used to assess the PSR effect on rocks.

5.3 Stress Path Coupling PSMV and PSR Effect

With the equations in Table 5, if q is formulated with the function of α , the complex stress path considering the PSMV and PSR effect can be simulated. Take a numerical loading simulation for an example. Hydrostatic pressure p was first loaded to 30 MPa, followed by the PSMV loading on the deviatoric plane with $q=40$ MPa, and $b=0.3$. The complex loading considering PSMV and PSR was finally applied. Here, for simplicity, q was presumed to have a linear relationship with α :

$$q = k_1\alpha + k_2 \tag{49}$$

where k_1 and k_2 are constants determined by the on-site conditions. In this example, we take $k_1=10$ MPa and $k_2=40$ MPa. Based on Eqs. (36) through (39), and (49), the stresses increment in the process are expressed as follows:

$$\Delta\sigma_z = \frac{3 \cos 2\dot{\alpha}t + 1 - 2b}{6\sqrt{b^2 - b + 1}}(k_1\dot{\alpha}t + k_2) \tag{50}$$

$$\Delta\sigma_r = \frac{2b - 1}{3\sqrt{b^2 - b + 1}}(k_1\dot{\alpha}t + k_2) \tag{51}$$

$$\Delta\sigma_\theta = \frac{-3 \cos 2\dot{\alpha}t + 1 - 2b}{6\sqrt{b^2 - b + 1}}(k_1\dot{\alpha}t + k_2) \tag{52}$$

$$\tau_{z\theta} = \frac{\sin 2\dot{\alpha}t}{2\sqrt{b^2 - b + 1}}(k_1\dot{\alpha}t + k_2) \tag{53}$$

where $\dot{\alpha}$ is the rotation rate of the major principal stress axis, and t is the loading time. In the loading test example, $\dot{\alpha}$ is set to $\pi/400$ per second. Figure 14 shows the controlling stresses and α in the coupling process. α and q increase in a linear manner over loading time. The principal stresses change throughout the process. This loading methodology can be used in engineering response simulations under complex stress application considering the coupling PSMV and PSR effect.

5.4 An Argumentation Based on Existing Theories

In the PSMV stress path, the vertical stress σ_z , radial stress σ_r , circumferential stress σ_θ is loaded to $p_0 + \Delta\sigma_z$, $p_0 + \Delta\sigma_r$ and $p_0 + \Delta\sigma_\theta$, respectively. In this way, assuming that the proposed

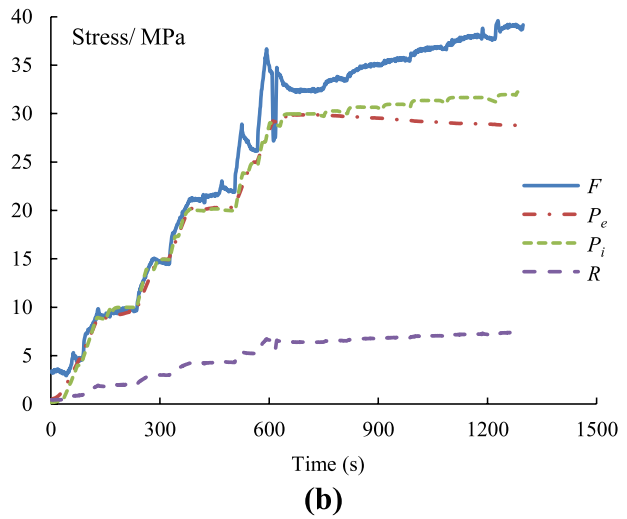
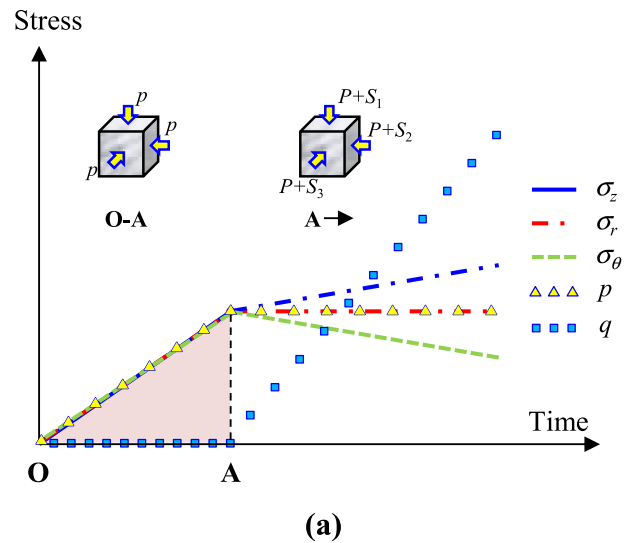
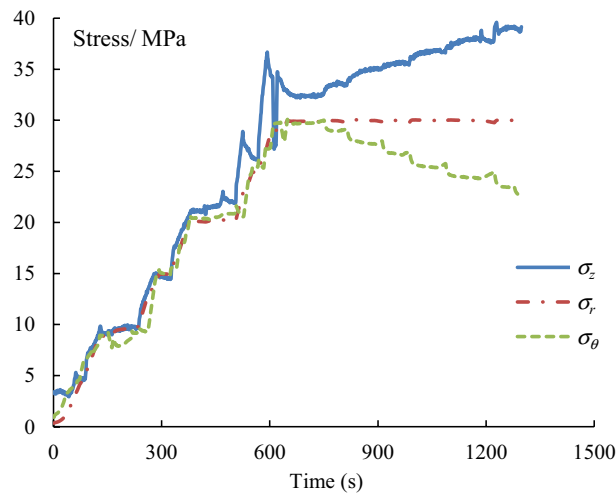


Fig. 12 Loads and stress variations in PSMV stress path: **a** expected stress path. **b** Load paths in the test. **c** Principal stress paths in the test. **d** Stress invariant path in the test

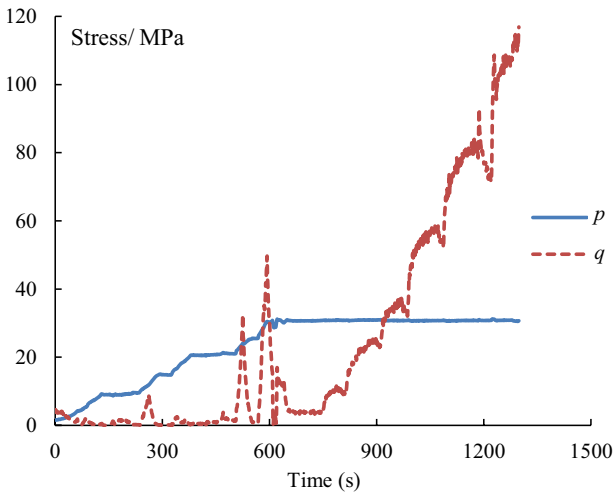
methodology is correct, $\Delta\sigma_z$, $\Delta\sigma_r$ and $\Delta\sigma_\theta$ should equal to the three principal stress deviators S_1, S_2 and S_3 , respectively.

From the Eqs. (16) and(21), the expression of $\Delta\sigma_z$ in Table 3 can be rewritten as:

$$\begin{aligned} \Delta\sigma_z &= \frac{2 - b}{3\sqrt{b^2 - b + 1}}q \\ &= \frac{2 - \frac{\sqrt{3}\tan\theta_\sigma + 1}{2}}{3\sqrt{\left(\frac{\sqrt{3}\tan\theta_\sigma + 1}{2}\right)^2 - \frac{\sqrt{3}\tan\theta_\sigma + 1}{2} + 1}}q \\ &= \frac{2}{3}q \cos\left(\theta_\sigma + \frac{\pi}{6}\right) \\ &= \frac{2}{\sqrt{3}}\sqrt{J_2} \cos\left(\theta_\sigma + \frac{\pi}{6}\right) \end{aligned} \tag{54}$$



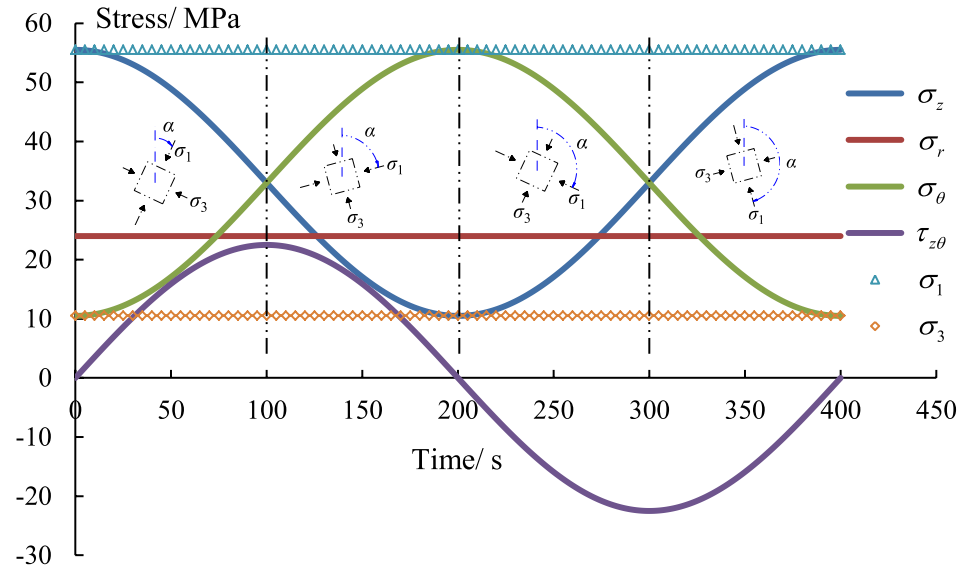
(c)



(d)

Fig. 12 (continued)

Fig. 13 The stresses variations in a PSR loading simulation

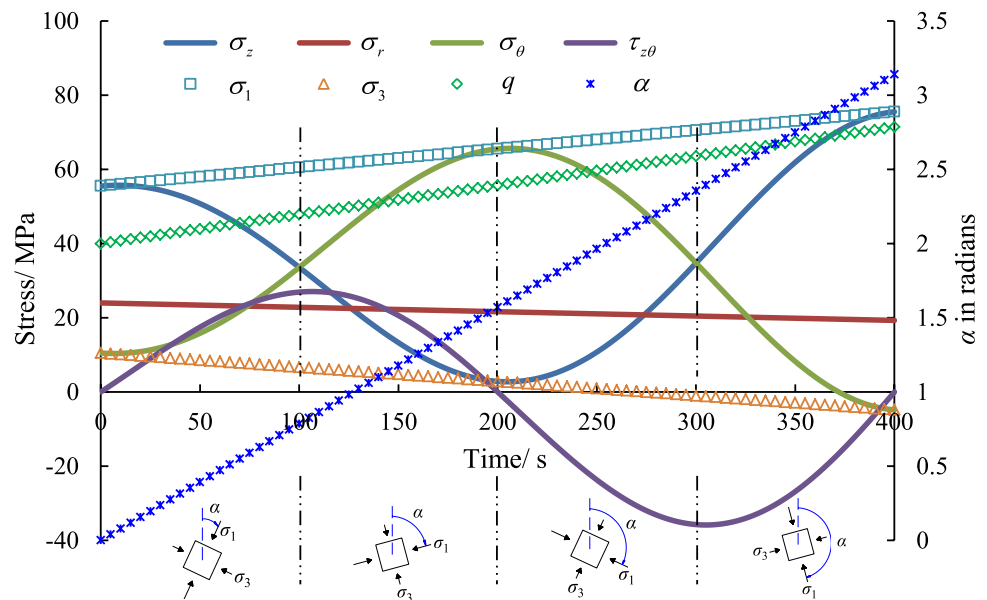


By the calculation of Eq. (54), $\Delta\sigma_z$ in Table 3 is observed to be identical to the expression of S_1 in Eq. (17). Similarly, by calculating $\Delta\sigma_r$ and $\Delta\sigma_\theta$ in Table 3, the same expressions as S_2 and S_3 in formulas (18) and (19) can be obtained, respectively. Therefore, the equations in Table 3 are verified suitable for PSMV stress path. Furthermore, because the expression in Table 3 is a special case of Table 5 when $\alpha=0$, the above analysis can indirectly prove the application of expressions in Table 5 to the stress path coupling PSMV and PSR effect. In other words, the methodology for stress path proposed in this paper is verified.

6 Conclusions

To address the dearth of research into stress control with HCA completing comprehensive stress path, we here investigated this methodology systematically. The elastic stresses distribution in the HCA sample and the equivalent stresses in the element were proposed. A mechanism for completing PSMV and PSR stress paths was sketched. The key to considering the PSR effect is applying a torque, which is represented by existence of a shear stress. Based on Mohr circle theory, the orientation angle of major principal stress was defined in an alternative prospect in Eq. (14). Using the above as foundation for the present work, the methodology for establishing comprehensive stress paths was investigated, including a hydrostatic pressure stress path [in Eq. (20)], PSMV stress path on the deviatoric plane (see Table 3), pure PSR stress path (see Table 4), and complex stress path coupling the PSMV and PSR effect (see Table 5). In the end, the proposed methodology for stress paths was verified using numerical simulations, case test and special case verification.

Fig. 14 Variations in stresses and α in a coupling loading simulation considering PSMV and PSR



The methodology for establishing a comprehensive stress path with the HCA was investigated systematically with respect to rock mechanics, contributing to the development of new HCAs and rock engineering simulations in complicated geological projects. The methodology for a comprehensive stress path, isolating the effect of stress invariants, is of great significance for studying the failure characteristics and the failure evolution of geomaterials. It is worth noting that the rock HCA is particularly suitable for studying the anisotropic mechanical properties of rock. Generally speaking, anisotropy consists of initial anisotropy and stress-induced anisotropy. The former is formed by geological reasons, while the latter is caused by stress disturbance (e.g., induced by artificial excavation). For the former, mechanical tests of rock samples with initial anisotropy can be carried out, while for the latter, different stress paths can be used in mechanical tests of isotropic rocks or intact rocks. Based on the method proposed in this paper, the strength and deformation characteristics in HCA tests and the mechanical model considering PSMV and PSR effects need to be further studied.

Acknowledgements We gratefully acknowledge financial support from the National Science Foundation of China (NSFC) (51704097, 51427803 and 51404240), the Scientific Instrument Developing Project of Chinese Academy of Sciences (YZ201553 and YZ201344), China National Key Basic Research Program under Grant No. 2014CB046902, the Key Opening Laboratory Project for Deep Mining Construction at Henan province (2015 KF-06), the Key Scientific Research Project of Henan Higher Education Institutions (16A560004) and Dr. Fund Projects of Henan Polytechnic University (B2016-65). Besides, the authors are also grateful to the editor Giovanni Barla and the anonymous reviewers for their many helpful comments, which have greatly improved this paper.

References

- Alsayed MI (2002) Utilising the Hoek triaxial cell for multiaxial testing of hollow rock cylinders. *Int J Rock Mech Min* 39(3):355–366
- Amann F, Button EA, Evans KF, Gischig VS, Blumel M (2011) Experimental study of the brittle behaviour of clay shale in rapid unconfined compression. *Rock Mech Rock Eng* 44(4):415–430
- Amann F, Kaiser PK, Button EA (2012) Experimental study of brittle behaviour of clay shale in rapid triaxial compression. *Rock Mech Rock Eng* 45(1):21–33
- Bieniawski ZT (1967) Mechanism of brittle fracture of rock. *Int J Rock Mech Min Sci* 4(4):395–430
- Cantiemi L, Anagnostou G (2009) The effect of the stress path on squeezing behavior in tunneling. *Rock Mech Rock Eng* 42(2):289–318
- Chen WF, Saleeb AF (2013) Constitutive equations for engineering materials: elasticity and modeling. Elsevier, Oxford
- Diederichs MS, Kaiser PK, Eberhardt E (2004) Damage initiation and propagation in hard rock during tunnelling and the influence of near-face stress rotation. *Int J Rock Mech Min* 41(5):785–812
- Ding Q, Ju F, Mao X, Ma D, Yu B, Song S (2016) Experimental investigation of the mechanical behavior in unloading conditions of sandstone after high-temperature treatment. *Rock Mech Rock Eng* 49(7):2641–2653
- Eberhardt E (2001) Numerical modelling of three-dimension stress rotation ahead of an advancing tunnel face. *Int J Rock Mech Min* 38(4):499–518
- Eberhardt E, Stead D, Stimpson B (1999) Quantifying progressive pre-peak brittle fracture damage in rock during uniaxial compression. *Int J Rock Mech Min Sci* 36(3):361–380
- Feng XT, Zhang X, Kong R, Wang G (2016) A novel Mogi type true triaxial testing apparatus and its use to obtain complete stress-strain curves of hard rocks. *Rock Mech Rock Eng* 49(5):1649–1662
- Fenner R (1938) Untersuchungen zur erkenntnis des gebirgsdrucks. *Glückauf* 32(74):681–695 (705–715)
- Ganne P, Vervoot A (2006) Characterisation of tensile damage in rock samples induced by different stress paths. *Pure Appl Geophys* 163(10):2153–2170

- Gutierrez M, Wang J, Yoshimine M (2009) Modeling of the simple shear deformation of sand: effects of principal stress rotation. *Acta Geotech* 4(3):193–201
- He MC, Miao JL, Feng JL (2010) Rock burst process of limestone and its acoustic emission characteristics under true-triaxial unloading conditions. *Int J Rock Mech Min* 47(2):286–298
- Hight DW, Gens A, Symes MJ (1983) The development of a new hollow cylinder apparatus for investigating the effects of principal stress rotation in soils. *Geotechnique* 33(4):355–383
- Ishihara K, Towhata I (1983) Sand response to cyclic rotation of principal stress directions as induced by wave loads. *Soils Found* 23(4):11–26
- Jiang MJ, Li QL, Yang QJ (2013) Experimental investigation on deformation behavior of TJ-1 lunar soil simulant subjected to principal stress rotation. *Adv Space Res* 52(1):136–146
- Kong YX, Yao YP, Zhao JD (2015) Modeling principal stress rotation for anisotropic sand. *Jpn Geotechn Soc Spec Publ* 1(2):22–27
- Lee DH, Juang CH, Chen JW, Lin HM, Shieh WH (1999) Stress paths and mechanical behavior of a sandstone in hollow cylinder tests. *Int J Rock Mech Min* 36(7):857–870
- Lee DH, Juang CH, Lin HM (2002) Yield surface of Mu-San sandstone by hollow cylinder tests. *Rock Mech Rock Eng* 35(3):205–216
- Lin QH, Yan JJ, Zhou J, Cao ZG (2016) Microstructure study on intact clay behavior subjected to cyclic principal stress rotation. *Procedia Eng* 143:991–998
- Ma XD, Rudnicki JW, Haimson BC (2017) Failure characteristics of two porous sandstones subjected to true triaxial stresses: applied through a novel stress path. *J Geophys Res Solid Earth* 122(4):2525–2540
- Miura K, Miura S, Toki S (1986) Deformation behavior of anisotropic dense sand under principal stress axes rotation. *Soils Found* 26(1):36–52
- Nishimura S, Towhata I (2004) A three-dimensional stress-strain model of sand undergoing cyclic rotation of principal stress axes. *Soils Found* 44(2):103–116
- O’Kelly BC, Naughton PJ (2005) Development of a new hollow cylinder apparatus for stress path measurements over a wide strain range. *Geotech Test J* 28(4):345–354
- O’Kelly BC, Naughton PJ (2009) Study of the yielding of sand under generalized stress conditions using a versatile hollow cylinder torsional apparatus. *Mech Mater* 41(3):187–198
- Predan J, Močilnik V, Gubeljak N (2013) Stress intensity factors for circumferential semi-elliptical surface cracks in a hollow cylinder subjected to pure torsion. *Eng Fract Mech* 105:152–168
- Saada AS, Fries G, Ker C (1983) An evaluation of laboratory testing techniques in soil mechanics. *Soils Found* 23(2):98–112
- Sayao A, Vaid YP (1991) A critical assessment of stress non-uniformities in hollow cylinder test specimens. *Soils Found* 3(1):60–72
- Sivathayalan S, Vaid YP (2002) Influence of generalized initial state and principal stress rotation on the undrained response of sands. *Can Geotech J* 39(1):63–76
- Talesnick ML, Katz A, Ringel M (2000) An investigation of the elastic stress-strain behavior of a banded sandstone and a sandstone-like material. *Geotech Test J* 23(3):257–273
- Vaid YP, Sayao A, Hou EH, Negussey D (1990) Generalized stress-path-dependent soil behavior with a new hollow cylinder torsional apparatus. *Can Geotech J* 27(5):601–616
- Wang Z, Yang Y, Yu H, Muraleetharan KK (2016) Numerical simulation of earthquake-induced liquefactions considering the principal stress rotation. *Soil Dyn Earthq Eng* 90:432–441
- Yang SQ (2016) Experimental study on deformation, peak strength and crack damage behavior of hollow sandstone under conventional triaxial compression. *Eng Geol* 213(4):11–24
- Yang SQ (2018) Fracturing mechanism of compressed hollow-cylinder sandstone evaluated by X-ray micro-CT scanning. *Rock Mech Rock Eng* 51(7):2033–2053
- Yang Y, Yu H (2013) A kinematic hardening soil model considering the principal stress rotation. *Int J Numer Anal Met* 37(13):2106–2134
- Zhang C, Zhou H, Feng XT, Xing L, Qiu SL (2011) Layered fractures induced by principal stress axes rotation in hard rock during tunnelling. *Mater Res Innov* 15:S527–S530
- Zhou XP (2010) Dynamic damage constitutive relation of mesoscopic heterogeneous brittle rock under rotation of principal stress axes. *Theor Appl Fract Mec* 54(2):110–116
- Zhou H, Jiang Y, Lu JJ, Gao Y, Chen J (2018) Development of a hollow cylinder torsional apparatus for rock. *Rock Mech Rock Eng*. <https://doi.org/10.1007/s00603-018-1563-5>

Publisher’s Note Springer Nature remains neutral with regard to jurisdictional claims in published maps and institutional affiliations.